A chemically inducible multimerization system for tunable and background-free RTK activation

Authors: Yuanmin Zheng[†1,2], Jinyu Fei[†1], Abhirup Chakrabarti[3], Ruobo Zhou[*1,2,3,4]

Affiliations: [1] Department of Chemistry, The Pennsylvania State University, University Park, PA 16802, USA

[2]Department of Biomedical Engineering, The Pennsylvania State University, University Park, PA 16802, USA

[3]Department of Biochemistry and Molecular Biology, The Pennsylvania State University, University Park, PA 16802, USA

[4]The Huck Institutes of Life Sciences, The Pennsylvania State University, University Park, PA 16802, USA

* To whom correspondence may be addressed. Email: ruobo.zhou@psu.edu

ABSTRACT

Receptor tyrosine kinases (RTKs) are key regulators of diverse cellular processes, including differentiation, migration, proliferation, survival, and intracellular communications, by transducing extracellular cues into intracellular responses. Upon oligomerization at the plasma membrane, RTKs become activated and initiate major downstream signaling cascades, such as the ERK pathway, which modulates cytoskeletal dynamics through phosphorylation of cytoskeletal regulators, regulation of actin-binding proteins, and transcriptional activation of immediate-early genes involved in cell structure and motility. Light-inducible RTK systems have been developed to achieve spatiotemporal control of RTK clustering and activation for both basic cell biology research and engineered applications, such as controlling cell migration, proliferation, or differentiation. However, these systems are limited by high basal RTK activation, where substantial RTK activation occurs even before induction, leading to unintended ERK activation and downstream effects. Here, we report a chemically inducible RTK system that minimizes basal activation while enabling direct visualization of RTK clustering at the plasma membrane upon induction. Single-cell imaging reveals visible RTK clusters after induction, with total RTK abundance in the clusters correlating with ERK phosphorylation levels. Using this system, we trigger an ERK-dependent, rapid disassembly of the spectrin-based membrane skeleton. In contrast to previous inducible RTK systems, where the membrane skeleton is disrupted even prior to induction due to background activation, our system exhibits disruption exclusively after induction, enabling precise dissection of RTK-mediated signaling events. This platform provides a powerful tool for dissecting RTK-mediated signaling dynamics and for engineering cell behaviors with accurate on-demand activation.

Introduction

Receptor tyrosine kinases (RTKs) comprise a structurally diverse family of transmembrane proteins that function as key regulators of cellular signaling, by converting extracellular stimuli into coordinated intracellular responses[1–4]. Ligand binding to RTKs induces conformational rearrangements that facilitate dimerization or higher-order multimerization of their cytoplasmic kinase domains, leading to autophosphorylation of specific tyrosine residues and subsequent recruitment of downstream signaling effectors[5,6]. Among the well-characterized downstream pathways of RTKs is the mitogen-activated protein kinase (MAPK) cascade, particularly the Raf–MEK–ERK axis, which governs essential cellular processes including proliferation, differentiation, morphogenesis, and cytoskeletal remodeling[7–9]. Notably, the amplitude and duration of ERK activation are highly sensitive to the spatial organization and clustering state of RTKs at the plasma membrane[10,11]. Parameters such as receptor density, oligomerization state and geometry, and subcellular localization may contribute to modulating downstream signaling strength in highly context-dependent manners[12,13].

Despite growing interest in controlling RTK clustering to modulate downstream cellular effects, such as controlling cell migration, proliferation, or differentiation, current tools for manipulating receptor multimerization remain limited in precision[14,15]. Optogenetic systems, particularly those based on Light-inducible oligomerization domains CRY2[16] or iLID[17], have been widely employed to induce RTK clustering in a light-dependent manner. However, these platforms often exhibit substantial basal activation even in the absence of light illumination[18], which is further exacerbated at high expression levels, owing to the intrinsic tendency of light-inducible oligomerization domains to self-associate. This leaky activation complicates quantitative analyses of downstream signaling, such as resolving dose–response relationships or defining kinetic thresholds with high confidence. Moreover, optogenetic activation requires continuous or repeated light illumination, which can introduce phototoxic effects and prove impractical in certain *in vivo* contexts. Chemically induced dimerization (CID) systems, such as rapamycin-mediated pairing of FK506-binding protein (FKBP) and the FKBP–rapamycin binding (FRB) domain of mTOR[19,20], offer a light-independent alternative for triggering RTK activation. However, conventional CID approaches are generally restricted to dimerization and do not support tunable higher-order assemblies, thereby limiting control over clustering geometry, valency, and spatial localization. These limitations underscore the need for a chemically controlled, modular system that enables background-free activation, and precise tunability, enabling detailed investigating of how RTK spatial organization translates into analog outputs such as ERK phosphorylation.

To overcome the limitations of existing RTK clustering tools, we developed a chemically inducible platform for precise control of RTK multimerization with minimal background activity, using fibroblast growth factor receptor 1 (FGFR1)[21–24] as a prototypical model receptor. Our system leverages rapamycin-mediated heterodimerization between FKBP

and FRB, a well-characterized CID pair that functions independently of light and exhibits rapid dimerization kinetics[2]. To achieve higher-order receptor clustering beyond simple dimerization, we integrated engineered oligomerization tags HOTag3 and HOTag6, two previously reported coiled-coil domains that assemble into hexametric and tetrameric complex, respectively[25,26]. By fusing the intracellular domain of FGFR1 to various combinations of FKBP/FRB and HOTag3/HOTag6 modules, we generated a library of chimeric receptor constructs with defined clustering geometries and subcellular localizations. Systematic evaluation revealed that configurations with membrane-anchored FGFR1-FKBP-HOTag6 paired with cytosolic FRB–HOTag3 supported strong rapamycin-inducible clustering while maintaining negligible basal ERK activation. For benchmarking, we compared our optimized constructs to reported CRY2-based optogenetic systems. Optogenetic FGFR1 systems based on the CRY2 variants—including wild type(WT)CRY2, CRY2olig[27] and optodroplet-forming CRY2 fusions[28]—exhibited considerable basal ERK activation even without light stimulation, consistent with the previously reported properties that CRY2 may exhibit some degree of self-association in the dark, even without light stimulation[29]. In contrast, our rapamycin-inducible system showed minimal basal ERK phosphorylation and robust, tunable activation upon rapamycin treatment. Live-cell imaging further confirmed that rapamycin rapidly induced spatially localized FGFR1 clustering, accompanied by recruitment of cytosolic components to the plasma membrane[30–33]. These optimized constructs enable on-demand, higher-order FGFR1 assembly that robustly triggers downstream ERK signaling. Importantly, the modular architecture of this system allows independent tuning of clustering localization, providing a versatile platform with significant advantages over existing optogenetic inducible approaches.

Using this modular chemical platform, we systematically investigated how the degree of FGFR1 clustering regulates ERK signaling in human cells. FGFR1 serves as an effective model system for studying the biophysical determinants of signal activation, due to its relevance in development and disease, and its pronounced sensitivity to multimerization[21–24]. The quantitative relationship between FGFR1 clustering degree and the resulting strength of ERK signaling remains unclear, posing an important challenge for both mechanistic studies of cell signaling and the rational engineering of synthetic signaling systems[21,24,34,35].

Our quantitative single-cell analysis showed that the extent of FGFR1 multimerization, measured by the total amount of FGFR1 molecules within FGFR1 clusters per cell, strongly correlated with phosphorylated ERK levels, establishing a proportional relationship between receptor clustering and downstream signaling amplitude.

To demonstrate the advantages of our optimized chemical-inducible RTK system, we utilized it to achieve the chemical inducible disassembly of the spectrin-based membrane skeleton in human cells[36,37]. Previous studies have shown that the spectrin-based membrane skeleton can be rapidly degraded following ERK activation[38,39]. Both widefield fluorescence and three-dimensional stochastic optical reconstruction microscopy (3D-STORM) imaging showed that rapamycin-induced FGFR1 clustering led to membrane

skeleton disassembly in cells expressing our chemical-inducible FGFR1 constructs, whereas untreated cells retained intact membrane skeleton structures. In contrast, cells expressing CRY2-based optogenetic systems exhibited membrane skeleton disassembly even without any light-stimulation. These findings confirm that our system enables precise control over ERK activity and can drive cytoskeletal remodeling as a downstream functional consequence. Together, these results establish our platform as a robust chemically inducible system for tuning RTK clustering and ERK activation with minimal basal activity.

Results

CRY2-based optogenetic FGFR1 constructs exhibits basal leaky ERK activation

Previously reported optogenetic RTK constructs have enabled light-inducible activation of downstream signaling cascades, including the MAPK/ERK pathway, with high spatiotemporal resolution[16]. Most of these systems utilize the CRY2-based clustering approach, which induces RTK oligomerization at the plasma membrane in response to blue light, thereby activating ERK cascades[40,41]. To evaluate the performance of CRY2-medicated clustering in regulating FGFR1 signaling, we tested three optogenetic FGFR1 constructs **(Fig. 1a)** with distinct clustering properties: 1) FGFR1-CRY2, in which cytoplasmic portion of FGFR1 (CytoFGFR1) is fused to wild-type CRY2; 2) FGFR1-CRY2oligo, incorporating the E490R[42] point mutation to enhance light-induced oligomerization; 3) FGFR1-Optodroplet, where Optodroplet" is a previously developed module combining wild-type CRY2 with a C-terminal tail and an intrinsically-disordered FUS domain to achieve light-induced formation of liquid condensates of the tagged protein via liquid-liquid phase separation[27,43]. All constructs were N-terminally tagged with a myristoylation (Myr) motif for membrane anchoring and fused to EGFP for fluorescence imaging.

U2OS cells transfected with the plasmids encoding each optogenetic FGFR1 construct were either exposed to blue light for 10 minutes or maintained in the dark, followed by phospho-ERK (p-ERK) quantification using a previously established immunofluorescence-based assay[44]. All three constructs—FGFR1–CRY2, FGFR1–CRY2olig, and FGFR1–Optodroplet—exhibited robust increases in p-ERK signal upon light stimulation, confirming that light-induced FGFR1 clustering activates the MAPK/ERK pathway **(Fig. 1b, right panels)**. However, we also observed elevated p-ERK signal in transfected cells maintained in the dark, compared to neighboring untransfected cells **(Fig. 1b, left panels)**. To more accurately quantify induced ERK activation, we calculated the total p-ERK fluorescence intensity at the single-cell level after background correction, where background was defined as the average total p-ERK fluorescence intensity in untransfected cells **(Fig. 1c)**. Statistical analysis revealed significant increases in p-ERK upon light stimulation for all constructs: FGFR1–CRY2 ($p = 5.92 \times 10^{-3}$), FGFR1–CRY2olig ($p = 1.37 \times 10^{-2}$), and FGFR1–Optodroplet ($p = 2.04 \times 10^{-3}$). However, elevated p-ERK levels in the unstimulated (light-) conditions, compared to the background p-ERK fluorescence determined from untransfected cells, suggest substantial basal leaky ERK activation without light illumination. Moreover, we

quantified the number of EGFP clusters per cell in the EGFP-channel to assess receptor multimerization. All three constructs showed a significant increase in FGFR1 cluster number per cell upon light stimulation **(Fig. 1d)**.

To further test whether the basal ("leaky") ERK activation observed with optogenetic FGFR1 multimerization depends which terminus of FGFR1 the light-inducible oligomerization domain CRY2 is fused to, and whether this effect also occurs with other RTKs, we generated additional constructs: 1) Optodroplet-FGFR1, in which the Optodroplet module was fused to the N-terminus of FGFR1 **(Fig. S1a,b)**; and 2) EphB2-optodroplet and optodroplet-EphB2, in which EphB2[45] is another well-studied RTK **(Fig. S1a,c)**. Quantification of ERK activity in cells expressing these constructs **(Fig. S1d)** revealed similarly elevated p-ERK levels without light illumination, indicating that leaky activation is not dependent on the CRY2 fusion site (N- vs. C-terminal) and is not restricted to FGFR1. These findings suggest that basal ERK activation is a general property of CRY2-based optogenetic RTK constructs in this context.

Together, these results indicate that CRY2-based RTK fusion proteins exhibit basal leaky ERK signaling, likely due to the intrinsic self-association propensity of CRY2. This effect is particularly pronounced in constructs containing the Optodroplet module. Membrane localization may further amplify clustering through two-dimensional confinement and increased local concentration[46]. Although blue light stimulation enhances RTK clustering and ERK signaling output, the elevated basal activity observed in the absence of light may limit the utility of CRY2-based optogenetic systems in contexts requiring a tight input–output coupling. These findings highlight the need for alternative systems with improved control over RTK multimerization and more stringent regulation of downstream signal induction.

Optimized rapamycin-inducible systems enable precise FGFR1 multimerization with minimal basal ERK activation

To circumvent the elevated basal activity observed with optogenetic FGFR1 constructs, we developed a novel chemically inducible system based on rapamycin-dependent heterodimerization of FKBP and FRB domains. Upon rapamycin addition, the FKBP–FRB pair rapidly associates with high affinity, enabling temporally precise induction of intracellular complex formation[47]. To promote higher-order clustering, we incorporated HOTag3 and HOTag6—two self-assembling peptide modules that form hexametric and tetrameric structures[26]. By fusing these elements to the intracellular domain of FGFR1, we designed a series of modular systems in which receptor multimerization could be tightly controlled, aiming to identify variants with low basal ERK activation in the absence of chemical stimulation **(Fig. 2a)**.

In the initial construct designs (Pair 1 and Pair 2), both interacting components consisted of membrane-anchored CytoFGFR1 fused to either FKBP-HOTag3 or FRB-HOTag6 **(Fig. S2, top panels)**. Pair 2 incorporated an additional intrinsically disordered FUS domain on both components to further enhance clustering propensity. Following rapamycin treatment, both pairs exhibited elevated levels of p-ERK, confirming activation of the

ERK pathway **(Fig. 2b, upper panels; Fig. 2c)**. However, substantial basal ERK activity was also observed in the absence of rapamycin stimulation, indicating that membrane anchoring of both components, combined with multimeric scaffolds, was sufficient to promote chemical-independent receptor clustering.

To mitigate the basal activation, we introduced a second set of constructs (Pairs 3–6) in which one of the two interacting components lacked the CytoFGFR1 domain but remained membrane-anchored via an N-terminal Myr motif **(Fig. 2a; Fig. S2, middle panels)**. This design aimed to reduce steric crowding while preserving rapamycin-inducible clustering capability. However, none of these pairs increased ERK phosphorylation upon rapamycin addition **(Fig. S3a; Fig. 3c)**, suggesting that they were unable to form signaling-competent receptor clusters. We speculate that tethering both components to the plasma membrane restricts conformational flexibility, thereby impeding the formation of productive oligomeric assembly[48], and that limited vertical mobility of membrane-anchored proteins may hinder efficient engagement between HOTag domains and downstream signaling adaptors.

To address the hypothesized factors that may have prevented rapamycin-induced clustering in Pairs 3-6, we implemented a third design strategy in which one interacting component was localized to the cytosol, while the other component remained a membrane-anchored CytoFGFR1 fusion (Pairs 7–10) **(Fig. 2a; Fig. S2, bottom panels)**. Among these pairs, Pair 8 and Pair 10 exhibited strong ERK activation upon rapamycin treatment with minimal basal signaling, producing robust increases in p-ERK levels **(Fig. 2b, bottom panels; Fig. 2c)**. In contrast, Pair 7 and Pair 9 displayed elevated p-ERK even without chemical stimulation **(Fig. S3b; Fig. 2c)**. Notably, in both pairs with high basal ERK background (i.e., Pair 7 and Pair 9), CytoFGFR1 was fused to HOTag3, a multimerization domain with higher valency than HOTag6. The increased basal activity observed in these constructs likely reflects enhanced spontaneous clustering driven by HOTag3, which has stronger self-association tendency. Together, these results highlight the importance of tuning both spatial asymmetry and multimerization strength to achieve precise, chemically inducible FGFR1 multimerization with minimal basal ERK activation.

Inducible FGFR1 clustering drives proportional ERK activation

The on-demand, background-free ERK activation observed for Pair 8 and Pair 10 constructs suggests that rapamycin induces FGFR1 multimerization. To directly monitor clustering dynamics in real time, we performed time-lapse live-cell imaging in U2OS cells expressing either Pair 8 or Pair 10 constructs **(Fig. 3a)**. Following rapamycin addition, both the EGFP-tagged FGFR1 component and the mScarlet-tagged cytosolic partner rapidly redistributed into discrete clusters that are colocalized in both color-channels. Quantitative image analysis revealed a significant increase in cluster number after stimulation, confirming efficient complex formation and receptor multimerization **(Fig. 3b)**. These results demonstrate that the system enables real-time, inducible control of FGFR1 clustering with high temporal precision.

To further investigate the relationship between receptor clustering and downstream ERK signaling strength, we examined how rapamycin-induced FGFR1 multimerization affected ERK activation at the single-cell level. Although previous experiments confirmed robust ERK phosphorylation following rapamycin stimulation with optimized construct configurations, it remained unclear whether variability in clustering efficiency across individual cells translates into proportional differences in signaling output. Fixed-cell immunofluorescence imaging of transfected U2OS cells revealed substantial heterogeneity in both cluster density and p-ERK fluorescence intensity across individual cells. Notably, cells with higher levels of receptor clustering exhibited stronger ERK phosphorylation, suggesting a potential quantitative relationship between FGFR1 multimerization and downstream ERK signaling. To systematically evaluate this relationship, we quantified cluster intensity and p-ERK fluorescence intensity across a large population of transfected cells **(Fig. 3c; Fig. S4a, b)**. Linear regression analysis revealed a strong positive correlation between the fluorescence intensity of p-ERK with the EGFP signal from the cluster (R^2 =0.712), which the total EGFP signal (R^2=0.382) and diffused EGFP signal (R^2=0.349) do not show a significant linear relationship, indicating that ERK activation scales proportionally with the extent of receptor multimerization in our rapamycin-inducible system.

Rapamycin-inducible RTK system enables on-demand, background-free membrane skeleton disassembly

To determine whether ERK activation mediated by our chemical-inducible RTK system elicits functional downstream effects and to highlight the advantage of its background-free activation, we assessed the structural integrity of the submembranous cytoskeleton before and after stimulation. βII-spectrin, a core component of the cortical cytoskeletal network, is known to be sensitive to ERK activity. Sustained ERK signaling has been shown to promote protease-dependent spectrin degradation in various cell types, including neurons and epithelial cells[9]. We hypothesized that if rapamycin-induced FGFR1 clustering activates ERK in a temporally sustained manner, it should lead to disruption of spectrin-based membrane skeleton.

We focused on Pair 8 and Pair 10 constructs, which exhibited the rapamycin-induced ERK activation with minimal basal ERK activity. U2OS cells expressing each pair were treated with rapamycin for 30 minutes, fixed, and immunostained for endogenous βII-spectrin. For each imaging field, both transfected and neighboring untransfected cells to enable direct side-by-side comparison of cytoskeletal architecture within the same local microenvironment **(Fig. 4a)**, thereby minimizing potential variability in cell density, substrate stiffness, and staining intensity across samples.

In the absence of rapamycin, both transfected and untransfected cells expressing Pair 8 or Pair 10 exhibited the expected spectrin immunostaining patterns, characterized by the puncta-like, heterogeneous islands of fluorescence located at the plasma membrane e. This organization is consistent with patterns reported in a previous study[49]. Following rapamycin stimulation, transfected cells displayed marked disruption of the spectrin-based membrane skeleton, where βII-spectrin fluorescence signal became diffuse,

homogeneously distributed, and reduced in intensity, lacking the characteristic membrane enrichment and spatial heterogeneity. In contrast, neighboring untransfected cells retained intact spectrin architecture, indicating that the observed disassembly in transfected cells was specifically triggered by FGFR1 activation rather than rapamycin alone. By comparison, cells transfected with optogenetic constructs or other rapamycin-inducible FGFR1 pairs exhibited spectrin disruption even prior to stimulation **(Fig. S5a)**, consistent with their elevated basal ERK activity.

To quantitatively assess the remodeling of spectrin membrane skeleton, we extracted two parameters from each cell: 1) mean βII-spectrin fluorescence intensity as a proxy for protein abundance **(Fig. 4b)**; and 2) mean coefficient of variation (CV) of pixel intensity to reflect spatial patterning **(Fig. 4c)**. Cells with intact spectrin architecture typically exhibit high CV values due to alternating regions of dense and sparse fluorescence, whereas disrupted networks display more homogeneous signal distribution and correspondingly lower CVs. In Pair 8, rapamycin-treated transfected cells exhibited a 25% reduction in spectrin intensity ($p = 1.02 \times 10^{-2}$) and a 30% decrease in CV ($p = 2.79 \times 10^{-2}$), consistent with substantial cytoskeletal disassembly. Similar trends were observed in Pair 10. In both cases, untransfected cells from the same imaging fields showed unchanged intensity and CV values before and after rapamycin treatment **(Fig. S5b)**, confirming that spectrin degradation was specifically linked to FGFR1 clustering and downstream ERK activation.

To further validate these observations at the nanoscale, we performed 3D-STORM super-resolution fluorescence imaging of βII-spectrin in cells expressing Pair 8 **(Fig. 4d)**. Without rapamycin, spectrin formed elongated, isolated islands along the inner leaflet of the plasma membrane, and within each island, a lattice-like arrangement of βII-spectrin molecular clusters was observed, similar to spectrin organization previously reported in neuronal soma[50] or red blood cells[51]. These elongated spectrin islands are consistent with exclusion patterns previously observed between the spectrin membrane skeleton and actin stress fibers in mouse embryonic fibroblast (MEF) cells[52,53]. After rapamycin treatment, these elongated spectrin islands disappeared, replaced by amorphous, isotropic, and markedly reduced density of βII-spectrin molecular clusters, consistent with cytoskeletal disassembly and loss of organized spectrin architecture.

Taken together, these results demonstrate that rapamycin-induced FGFR1 clustering leads to functionally relevant ERK activation, driving spectrin degradation and cytoskeletal remodeling. This effect was consistently observed across two independently optimized construct configurations, underscoring the robustness and reproducibility of the system. Notably, our chemical-inducible RTK platform shows no basal undesired induction compared to the existing inducible RTK systems. The integration of downstream functional readouts highlights the utility of this platform for probing how graded signal input strength governs cytoskeletal architecture.

Working model linking FGFR1 multimerization to ERK activation and spectrin degradation

To synthesize our findings and highlight the modularity and biological relevance of synthetic FGFR1 clustering, we developed a mechanistic model summarizing the observed behavior of both optogenetic and chemically inducible systems **(Fig. 5)**. This schematic compares the modes of receptor multimerization, corresponding ERK signaling profiles, and downstream cellular outcomes.

On the left, we depict CRY2-based optogenetic FGFR1 constructs. Upon blue light stimulation, CRY2 oligomerizes to induce FGFR1 clustering and activate downstream ERK pathway. However, due to the intrinsic self-association properties of CRY2—particularly in high-expression contexts or in variants containing oligomerization-promoting mutations (CRY2olig) or intrinsically-disordered domains (e.g., FUS)—substantial basal clustering and ERK activation occur even in the absence of light. This leakiness limits the dynamic range and compromises control over tight input–output relationships.

On the right, we illustrate the rapamycin-inducible clustering system. In this design, rapamycin addition triggers heterodimerization between FKBP- and FRB-tagged components, bringing multimerization domains (HOTag3 or HOTag6) into proximity to drive FGFR1 clustering. By leveraging spatial asymmetry—for example, pairing membrane-localized FGFR1–HOTag6 with cytosolic HOTag3–FKBP—we achieved minimal basal ERK activity and robust, tunable ERK activation upon stimulation. This configuration affords precise temporal control and low background activation.

Importantly, the model incorporates the downstream biological outcome of ERK activation: βII-spectrin degradation and cortical cytoskeletal disassembly, as confirmed by both widefield and 3D-STORM fluorescence imaging. The reproducible construct performance underscores the system's capacity for fine-tuned modulation of signal-dependent cytoskeletal remodeling.

Overall, this working model highlights the design flexibility and signaling fidelity of chemically inducible clustering platforms, offering a powerful framework for interrogating how spatial and valency-based parameters encode biological responses.

Conclusions

Precise modulation of RTK clustering remains a central objective in cell signaling research, as receptor multimerization serves as a key regulatory node linking extracellular ligand engagement to downstream biochemical and mechanical outputs[4]. In this study, we developed and characterized a chemically inducible system for FGFR1 clustering based on rapamycin-induced FKBP-FRB heterodimerization[54,55], in combination with the modular multimerization domain HOTag3 and HOTag6[25]. Through systematic construct design and comparative functional analysis, we demonstrate that this platform enables tightly controllable, low-background activation of the ERK signaling cascade. Furthermore, we show that ERK activation through this inducible clustering system produces functional downstream effects that extend to nanoscale remodeling of the cortical cytoskeleton, as evidenced by spectrin disassembly and loss of cytoskeletal organization.

By directly comparing our rapamycin-inducible system with conventional CRY2-based optogenetic approaches, we identified several key distinctions. Although CRY2 oligomerization has been widely utilized to control RTK clustering[56], our results show that it is associated with substantial basal ERK activity, even in the absence of light. This leaky behavior is particularly pronounced in engineered variants containing CRY2olig or CRY2cluster domain, where intrinsic self-association or phase separation promotes spontaneous receptor clustering independent of external light stimulation. In contrast, our optimized rapamycin-inducible constructs—specifically Pairs 8 and 10—exhibited minimal background ERK signaling and robust ERK activation following rapamycin treatment, demonstrating superior signaling fidelity and dynamic range.

To confirm that synthetic ERK activation elicits biologically relevant outcomes and to demonstrate the advantage of our background-free design in controlling these outcomes, we examined βII-spectrin, a key structural component of the membrane-associated cytoskeleton known to be destabilized by ERK signaling. In cells expressing either Pair 8 or Pair 10 constructs, rapamycin treatment resulted in a significant reduction in spectrin intensity and spatial heterogeneity, as quantified by mean immunofluorescence intensity and coefficient of variation. Importantly, these effects were restricted to transfected cells and absent in adjacent untransfected controls, indicating that cytoskeletal remodeling was specifically induced by receptor activation and downstream signaling. In contrast, previous inducible RTK designs with basal ERK activation exhibited spectrin disruption even prior to stimulation. Super-resolved 3D-STORM imaging further revealed the loss of organized spectrin islands following stimulation, confirming that the system is sufficient to drive nanoscale cytoskeletal reorganization. Together, these findings establish a direct link between receptor clustering, ERK activation, and cytoskeletal integrity, and demonstrate that the synthetic clustering platform can produce functional outputs relevant to cellular architecture.

While our system enables robust and tunable ERK activation, its dependence on the irreversible FKBP–FRB interaction limits temporal reversibility. To expand its versatility, future iterations may incorporate reversible dimerization modules, such as photoactivatable chemical inducers or ligand-binding systems with fast dissociation kinetics. Moreover, the platform can be readily adapted to investigate additional ERK-regulated processes, including transcriptional programs, metabolic pathways, and cytoskeletal dynamics involving myosin motors or actin crosslinking proteins. These extensions would further enhance the system's utility for dissecting ERK signaling networks in a modular, controllable, and pathway-specific manner.

The modular architecture of this system allows for broad applicability to other RTKs and membrane-associated signaling complexes. By substituting FGFR1 with alternative receptors—such as TrkA/B, VEGFR, or synthetic RTK chimeras[57–59], it will be possible to further investigate how clustering geometry, valency, and membrane localization influence signaling specificity and temporal dynamics. In addition, coupling this platform with spatially restricted rapamycin or optochemogenetic actuators could enable subcellular control of receptor clustering with precision comparable to optogenetic tools, while

maintaining the advantage of low basal activation. These extensions would further expand the utility of this system for dissecting compartmentalized signaling networks with high spatial and temporal fidelity.

Beyond single-cell analyses, this system holds promise for use in multicellular and organoid models, where spatiotemporally controlled receptor clustering could enable investigation of morphogen gradients, cell–cell communication, and tissue-level patterning. Its compatibility with live-cell imaging further enhances its utility in complex biological systems. Moreover, our observation that synthetic FGFR1 clustering leads to spectrin disassembly suggests broader applications for studying signal-to-mechanical feedback loops[60], with potential implications for epithelial barrier integrity, neuronal polarity, and cancer cell plasticity.

In summary, this study presents a chemically tunable, and functionally robust platform for RTK clustering with minimal background activation. The system enables mechanistic dissection of the causal relationship between receptor organization, signaling strength, and downstream cellular architecture. By integrating precise spatial control with modular design, it offers a versatile framework for probing and engineering signal transduction pathways with molecular precision.

Author contributions

R.Z. conceived the project. Y.Z., J.F., and R.Z. designed experiments, interpreted the data and wrote the manuscript. Y.Z., J.F., A.C. performed experiments. Y.Z. and J.F. analyzed the data. R.Z. supervised the project.

Conflicts of interest

There are no conflicts to declare.

Data availability

All data supporting the findings of this study are provided within the paper and its supplemental information.

Custom Python and MATLAB codes for image acquisition and STORM analysis are available at

https://github.com/ZhuangLab (DOI: 10.5281/zenodo.3264857)

Other custom MATLAB codes used in this study are available from the corresponding authors upon reasonable request.

Acknowledgements

This work was supported by National Institute of General Medical Sciences (R35GM142973), the Life Sciences Research Foundation, and the startup fund from the Pennsylvania State University provided to R.Z.

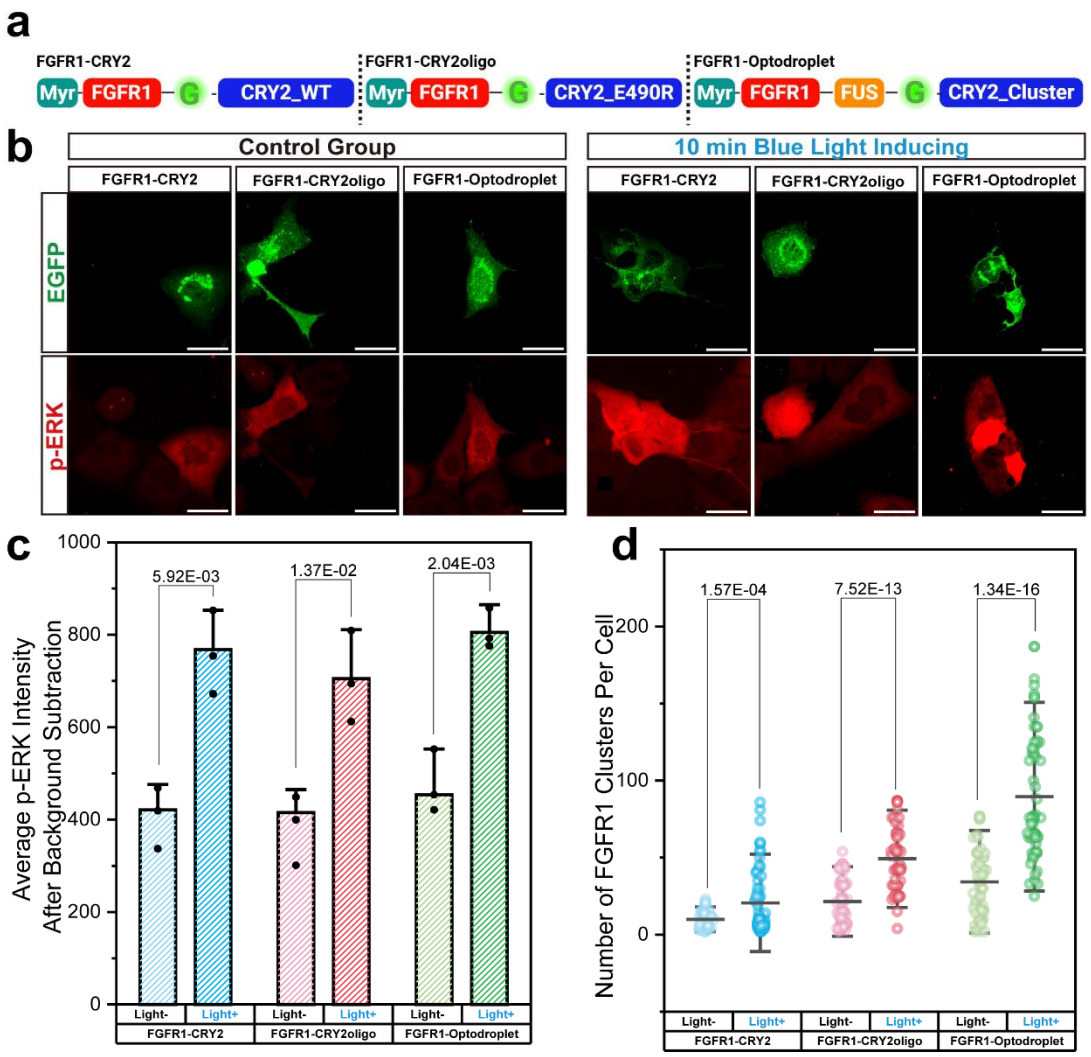

Fig. 1 CRY2-based optogenetic clustering of FGFR1 activates ERK signaling

a, Schematic diagrams of three optogenetic FGFR1 constructs: FGFR1–CRY2 (wild-type CRY2), FGFR1–CRY2olig (harboring the E490R oligomerization-enhancing mutation), and FGFR1–Optodroplet (CRY2 fused to the intrinsically disordered FUS domain). All constructs include an N-terminal myristoylation (Myr) motif for membrane anchoring and

a EGFP fluorophore for fluorescence imaging. **b,** Representative confocal immunofluorescence images of fixed U2OS cells expressing each construct under control (no light) or blue light stimulation (for 10 min). EGFP signal (green) indicates FGFR1 expression and localization; p-ERK signal (red) was detected by immunostaining. Scale bars, 10 μm. **c,** Quantification of average total p-ERK fluorescence intensity in individual transfected cells with or without light stimulation. Background p-ERK fluorescence values were obtained from neighboring untransfected cells and subtracted. Data represent mean ± s.d. from three independent experiments. p-values were determined by two-sided Student's t-test. **d,** Quantification of FGFR1 cluster number per cell with or without light stimulation for each construct, used as a measure for the degree of FGFR1 clustering. Each data point represents an individual cell; Horizontal bars indicate means with s.d.). p-values are calculated using two-sided Student's t-test.

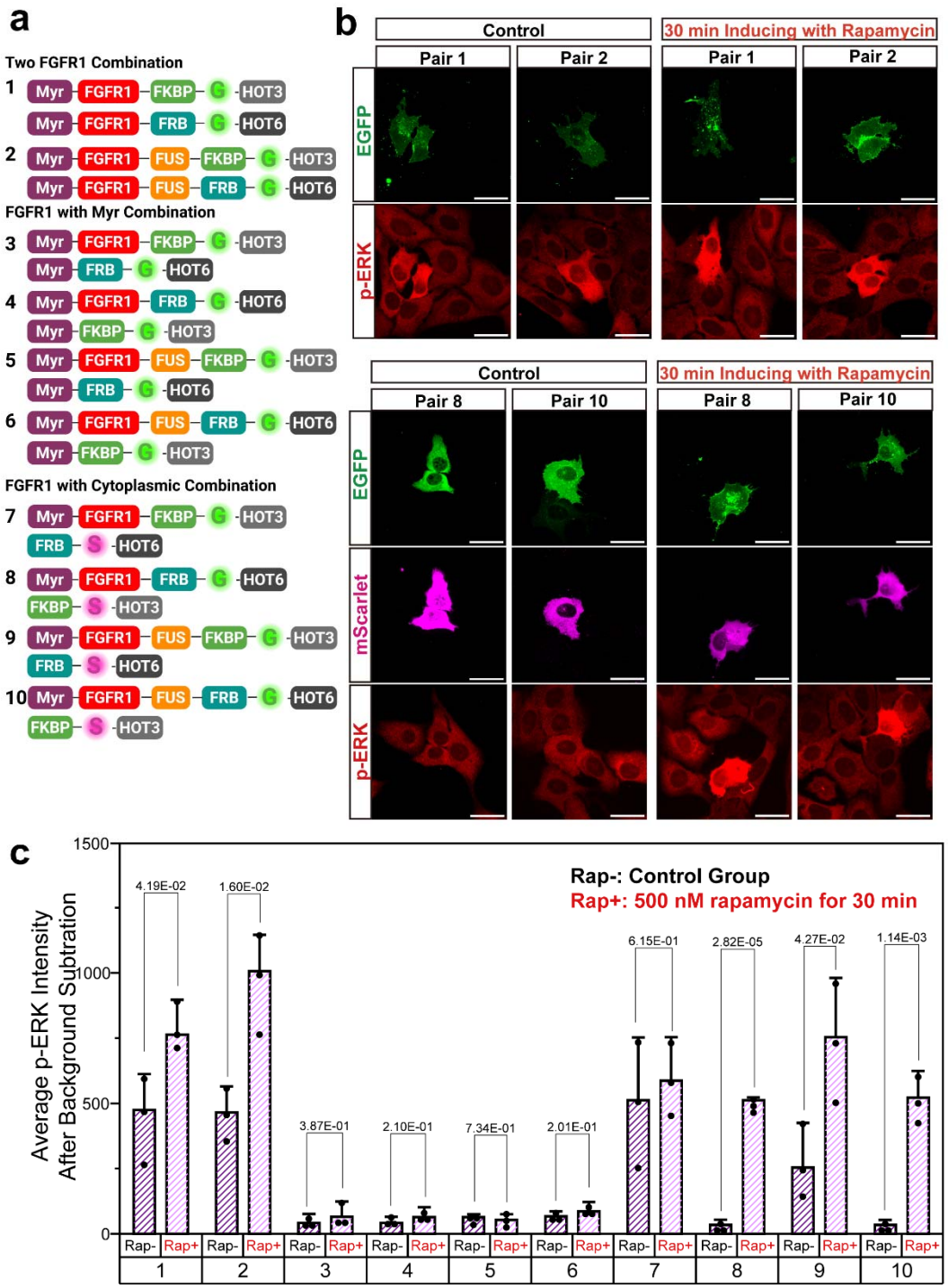

Fig. 2 Systematic design and screening for rapamycin-inducible FGFR1 clustering construct with minimal basal ERK activation

a, Schematic diagrams of all ten construct pairs (Pairs 1–10) designed to evaluate rapamycin-inducible FGFR1 clustering. Each pair consists of membrane-anchored or cytosolic components fused to FKBP or FRB domains, along with multimerization

domains HOTag3 (HOT3) or HOTag6 (HOT6), and, in some cases, the intrinsically disordered FUS domain. FGFR1 fusions are indicated in red; Myr denotes N-terminal myristoylation motif for membrane localization; G and S represent fluorescence protein EGFP and mScarlet. **b,** Representative fixed-cell confocal immunofluorescence images of U2OS cells expressing each construct pair, under either unstimulated (Control) or rapamycin-treated (500 nM for 30 min) conditions. EGFP (green) and mScarlet (magenta) indicate expression and localization of the FGFR1 fusion and its partner, respectively. Phosphorylated ERK (p-ERK; red) was visualized through immunostaining. Scale bars, 10 μm. **c,** Quantification of average total p-ERK fluorescence intensity in transfected cells across all ten construct pairs, with or without rapamycin treatment. p-ERK intensity values were background-subtracted using adjacent untransfected cells. Bars represent mean ± s.d. from three biological replicates. p-values were calculated using a two-sided unpaired Student's t-test.

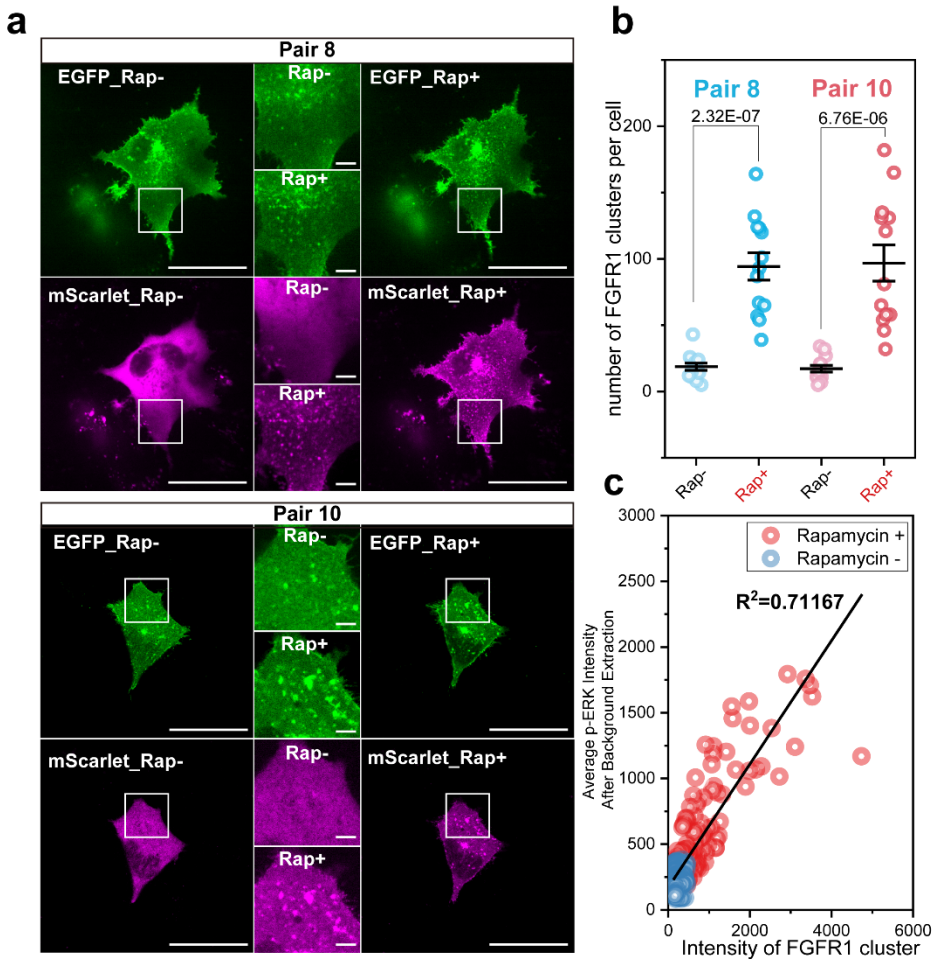

Fig. 3 Rapamycin-induced FGFR1 clustering correlates with ERK pathway activation at single-cell level

a, Representative live-cell confocal images of U2OS cells expressing construct pair 8 (top) or pair 10 (bottom), imaged before (Rap−) and after (Rap+) treatment with 500 nM rapamycin for 30 minutes. EGFP (green) labels membrane-tethered FGFR1 fusion construct and mScarlet (magenta) labels the cytosolic multimerization partner. Insets show magnified views of FGFR1 clustering following stimulation. Scale bars, 10 µm. **b,** Quantification of the number of clusters per cell that are colocalized in both color channels before and after rapamycin treatment for Pair 8 and Pair 10. Each point represents an individual cell. Bars represent mean ± s.d. from three biological replicates. p-values were calculated using a two-sided Mann–Whitney U test. **c,** Correlation between total fluorescence intensity within the clusters and total p-ERK fluorescence intensity across individual cells. Linear regression analysis shows a strong positive correlation ($R^2 = 0.71167$), indicating that ERK activation scales proportionally with the extent of FGFR1 clustering.

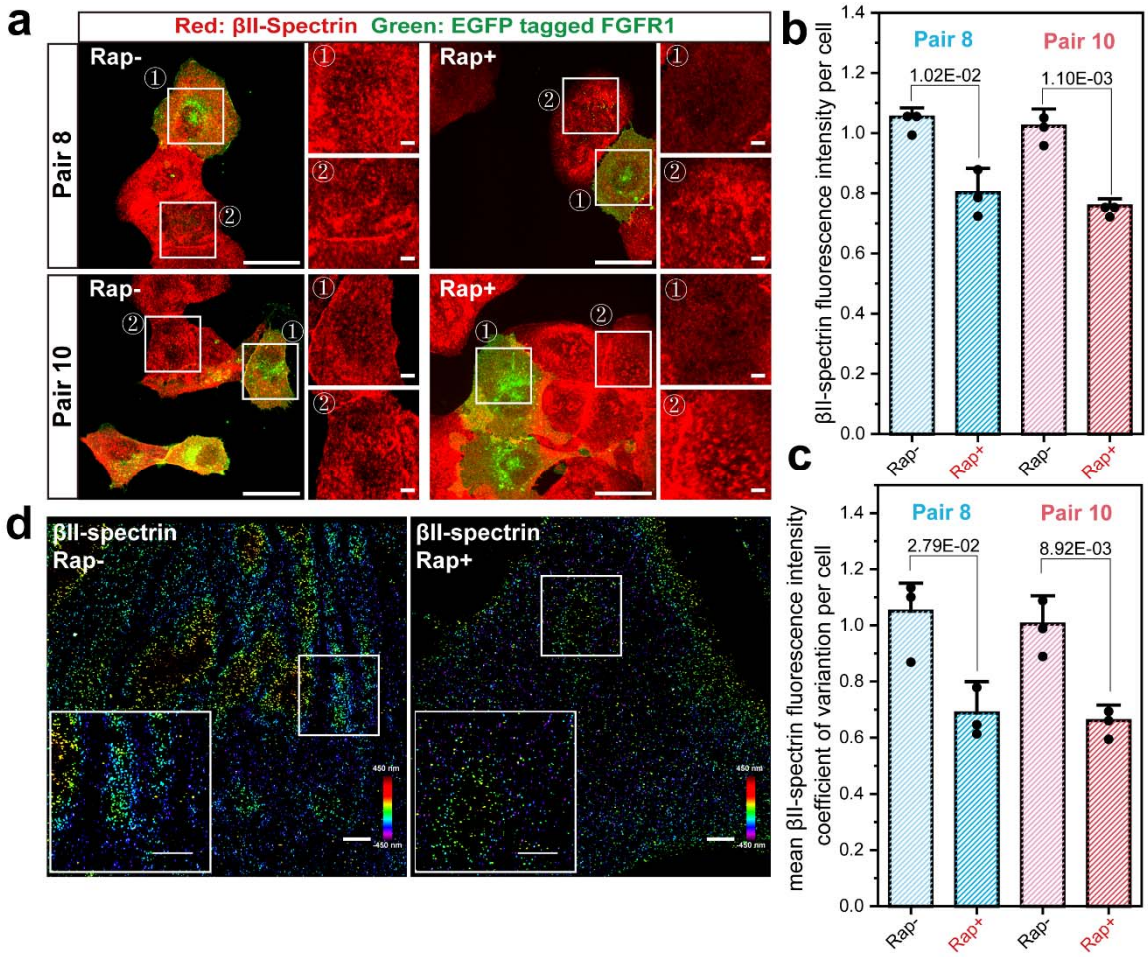

Fig. 4 Controlled, background-free disassembly of the spectrin-based membrane skeleton via our rapamycin-inducible system

a, Representative widefield immunofluorescence images of U2OS cells expressing Pair 8 (top) or Pair 10 (bottom) constructs, without (Rap−) or with 500 nM rapamycin treatment (Rap+) for 30 minutes. βII-spectrin was visualized with immunostaining in red, and EGFP-tagged FGFR1 constructs are shown in green. Insets show zoomed-in regions of transfected ① and neighboring untransfected ② cells from the same field of view. Spectrin organization is markedly disrupted in transfected cells after rapamycin stimulation but remains intact in adjacent untransfected cells. Scale bars, 10 μm. **b,** Quantification of mean βII-spectrin fluorescence intensity per cell under each condition. Data represent mean ± s.d. from three biological replicates. p-values are calculated using a two-sided unpaired Student's T-test. **c,** mean coefficient of variation (CV) of βII-spectrin fluorescence intensity, used as a proxy for spatial heterogeneity and cytoskeletal patterning. Cells with intact spectrin networks exhibit high CVs due to alternating bright/dark regions, and spectrin-disrupted cells show reduced CV. Values are mean ± s.d. from three biological replicates. p-values are calculated using a two-sided unpaired

Student's T-test. **d,** 3D-STORM super-resolution images of βII-spectrin in U2OS cells expressing Pair 8, treated with or without 500 nM rapamycin for 30 minutes. In control cells (Rap−), spectrin forms continuous, fiber-like structures aligned with the plasma membrane. In rapamycin-treated cells (Rap+), spectrin signal becomes diffuse and isotropic, lacking structured meshwork. The z-positions in the STORM images are color-coded according to the color scale, with violet and red indicating positions closest to and farthest from the substratum, respectively. Scale bars, 2 μm (Original), 2 μm (Cropped).

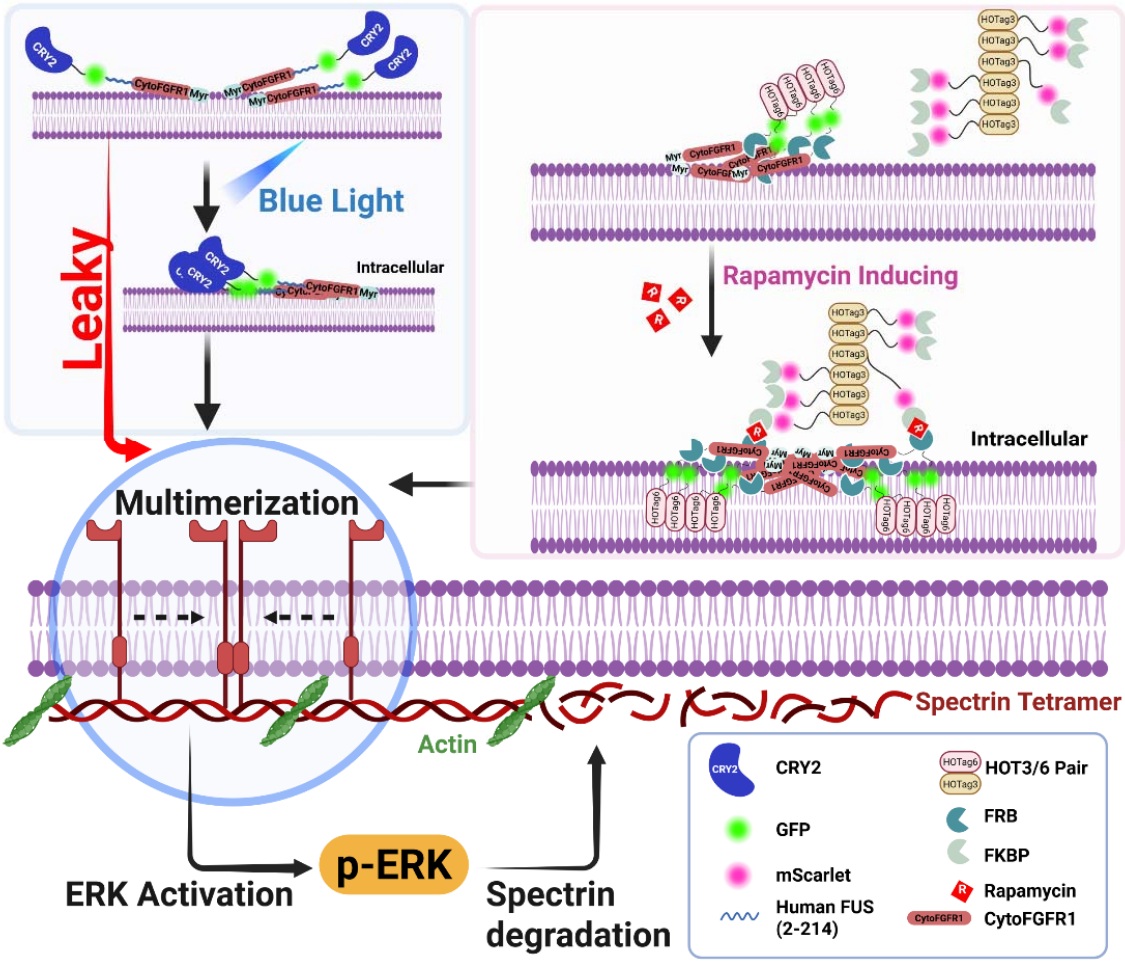

Fig. 5 Mechanistic model comparing optogenetic and chemically inducible RTK clustering systems

Schematic illustrating the molecular architecture, activation mechanism, and functional consequences of CRY2-based optogenetic versus rapamycin-inducible FGFR1 clustering systems. Left (blue panel): CRY2-fused FGFR1 constructs undergo light-induced oligomerization, promoting FGFR1 clustering and ERK activation. However, CRY2's intrinsic self-association propensity—particularly in oligomerization-enhancing mutants or phase-separating variants—leads to receptor clustering and ERK activation even in the absence of light (leaky activation), compromising input-output precision. Right (purple panel): In the rapamycin-inducible system, multimerization is triggered through rapamycin-mediated heterodimerization of FKBP and FRB, which assemble FGFR1 tethered to higher-order HOTag3 and HOTag6 oligomers. This configuration yields tunable confined clustering with minimal background activity. Bottom: In both systems, receptor clustering promotes ERK phosphorylation, which in turn drives disassembly of

the cortical spectrin-based membrane skeleton, This effect was confirmed by both widefield and 3D-STORM fluorescence imaging in rapamycin-treated cells. Spectrin degradation is represented as a downstream functional consequence of ERK activation. Key components are color-coded and summarized in the inset legend (bottom right). Created in BioRender. Zheng, Y. (2025) https://BioRender.com/gxkzrjo

References

1. Tomuleasa, C. *et al.* Therapeutic advances of targeting receptor tyrosine kinases in cancer. *Signal Transduct. Target. Ther.* **9**, 201 (2024).
2. Casaletto, J. B. & McClatchey, A. I. Spatial regulation of receptor tyrosine kinases in development and cancer. *Nat. Rev. Cancer* **12**, 387–400 (2012).
3. Du, Z. & Lovly, C. M. Mechanisms of receptor tyrosine kinase activation in cancer. *Mol. Cancer* **17**, 58 (2018).
4. Lemmon, M. A. & Schlessinger, J. Cell signaling by receptor tyrosine kinases. *Cell* **141**, 1117–1134 (2010).
5. Trenker, R. & Jura, N. Receptor Tyrosine Kinase activation: from the ligand perspective. *Curr. Opin. Cell Biol.* **63**, 174–185 (2020).
6. Maruyama, I. N. Mechanisms of Activation of Receptor Tyrosine Kinases: Monomers or Dimers. *Cells* **3**, 304–330 (2014).
7. Bahar, M. E., Kim, H. J. & Kim, D. R. Targeting the RAS/RAF/MAPK pathway for cancer therapy: from mechanism to clinical studies. *Signal Transduct. Target. Ther.* **8**, 455 (2023).
8. Pratilas, C. A. & Solit, D. B. Targeting the mitogen-activated protein kinase pathway: physiological feedback and drug response. *Clin. Cancer Res. Off. J. Am. Assoc. Cancer Res.* **16**, 3329–3334 (2010).
9. Zhou, R., Han, B., Xia, C. & Zhuang, X. Membrane-associated periodic skeleton is a signaling platform for RTK transactivation in neurons. *Science* **365**, 929–934 (2019).
10. Sammons, R. M., Ghose, R., Tsai, K. Y. & Dalby, K. N. Targeting ERK beyond the boundaries of the kinase active site in melanoma. *Mol. Carcinog.* **58**, 1551–1570 (2019).
11. Ho, E. K. *et al.* A live-cell biosensor of *in vivo* receptor tyrosine kinase activity reveals feedback regulation of a developmental gradient. *Cell Rep.* **44**, 115930 (2025).
12. Stangl, M. & Schneider, D. Functional competition within a membrane: Lipid recognition *vs.* transmembrane helix oligomerization. *Biochim. Biophys. Acta BBA - Biomembr.* **1848**, 1886–1896 (2015).
13. Paul, M. D. & Hristova, K. The RTK Interactome: Overview and Perspective on RTK Hetero-Interactions. *Chem. Rev.* **119**, 5881–5921 (2019).
14. Kramer, M. M., Lataster, L., Weber, W. & Radziwill, G. Optogenetic Approaches for the Spatiotemporal Control of Signal Transduction Pathways. *Int. J. Mol. Sci.* **22**, 5300 (2021).
15. Pal, A. A. *et al.* Optogenetic clustering and membrane translocation of the BcLOV4 photoreceptor. *Proc. Natl. Acad. Sci. U. S. A.* **120**, e2221615120.
16. Leopold, A. V. & Verkhusha, V. V. Light control of RTK activity: from technology development to translational research. *Chem. Sci.* **11**, 10019–10034 (2020).
17. Hope, J. M., Liu, A., Calvin, G. J. & Cui, B. Construction of Light-Activated Neurotrophin Receptors Using the Improved Light-Induced Dimerizer (iLID). *J. Mol. Biol.* **432**, 3739–3748 (2020).
18. Pathak, G. P. *et al.* Bidirectional approaches for optogenetic regulation of gene expression in mammalian cells using Arabidopsis cryptochrome 2. *Nucleic Acids Res.* **45**, e167 (2017).
19. Deane, C. Three's company. *Nat. Chem. Biol.* **16**, 1037–1037 (2020).

20. Inobe, T. & Nukina, N. Rapamycin-induced oligomer formation system of FRB–FKBP fusion proteins. *J. Biosci. Bioeng.* **122**, 40–46 (2016).
21. Edirisinghe, O., Ternier, G., Alraawi, Z. & Suresh Kumar, T. K. Decoding FGF/FGFR Signaling: Insights into Biological Functions and Disease Relevance. *Biomolecules* **14**, 1622 (2024).
22. Blum, Y. *et al.* Temporal perturbation of ERK dynamics reveals network architecture of FGF2/MAPK signaling. *Mol. Syst. Biol.* **15**, e8947 (2019).
23. Latko, M. *et al.* Cross-Talk between Fibroblast Growth Factor Receptors and Other Cell Surface Proteins. *Cells* **8**, 455 (2019).
24. Ibrahimi, O. A., Zhang, F., Lang Hrstka, S. C., Mohammadi, M. & Linhardt, R. J. Kinetic Model for FGF, FGFR, and Proteoglycan Signal Transduction Complex Assembly. *Biochemistry* **43**, 4724–4730 (2004).
25. Mumford, T. R. *et al.* Simple visualization of submicroscopic protein clusters with a phase-separation-based fluorescent reporter. *Cell Syst.* **15**, 166-179.e7 (2024).
26. Zhang, Q. *et al.* Visualizing Dynamics of Cell Signaling In Vivo with a Phase Separation-Based Kinase Reporter. *Mol. Cell* **69**, 334-346.e4 (2018).
27. Taslimi, A. *et al.* An optimized optogenetic clustering tool for probing protein interaction and function. *Nat. Commun.* **5**, 4925 (2014).
28. Kim, N. *et al.* Spatiotemporal Control of Fibroblast Growth Factor Receptor Signals by Blue Light. *Chem. Biol.* **21**, 903–912 (2014).
29. Zeng, D., Lv, J., Li, X. & Liu, H. The Arabidopsis blue-light photoreceptor CRY2 is active in darkness to inhibit root growth. *Cell* **188**, 60-76.e20 (2025).
30. Bennett, V. & Healy, J. Membrane Domains Based on Ankyrin and Spectrin Associated with Cell–Cell Interactions. *Cold Spring Harb. Perspect. Biol.* **1**, a003012 (2009).
31. Unsain, N., Stefani, F. D. & Cáceres, A. The Actin/Spectrin Membrane-Associated Periodic Skeleton in Neurons. *Front. Synaptic Neurosci.* **10**, (2018).
32. Han, B., Zhou, R., Xia, C. & Zhuang, X. Structural organization of the actin-spectrin–based membrane skeleton in dendrites and soma of neurons. *Proc. Natl. Acad. Sci.* **114**, E6678–E6685 (2017).
33. Hotulainen, P. & Lappalainen, P. Stress fibers are generated by two distinct actin assembly mechanisms in motile cells. *J. Cell Biol.* **173**, 383–394 (2006).
34. Porębska, N. *et al.* Targeting Cellular Trafficking of Fibroblast Growth Factor Receptors as a Strategy for Selective Cancer Treatment. *J. Clin. Med.* **8**, 7 (2018).
35. Pozniak, M. *et al.* FGFR1 clustering with engineered tetravalent antibody improves the efficiency and modifies the mechanism of receptor internalization. *Mol. Oncol.* **14**, 1998–2021 (2020).
36. Lorenzo, D. N., Edwards, R. J. & Slavutsky, A. L. Spectrins: molecular organizers and targets of neurological disorders. *Nat. Rev. Neurosci.* **24**, 195–212 (2023).
37. Ghisleni, A. *et al.* Complementary mesoscale dynamics of spectrin and acto-myosin shape membrane territories during mechanoresponse. *Nat. Commun.* **11**, 5108 (2020).
38. Zhou, R., Han, B., Xia, C. & Zhuang, X. Membrane-associated periodic skeleton is a signaling platform for RTK transactivation in neurons. *Science* **365**, 929–934 (2019).
39. Zhou, R. *et al.* Proteomic and functional analyses of the periodic membrane skeleton in neurons. *Nat. Commun.* **13**, 3196 (2022).

40. Kim, N. *et al.* Spatiotemporal control of fibroblast growth factor receptor signals by blue light. *Chem. Biol.* **21**, 903–912 (2014).
41. Zhang, K. & Cui, B. Optogenetic control of intracellular signaling pathways. *Trends Biotechnol.* **33**, 92–100 (2015).
42. Duan, L. *et al.* Understanding CRY2 interactions for optical control of intracellular signaling. *Nat. Commun.* **8**, 547 (2017).
43. Shin, Y. & Brangwynne, C. P. Liquid phase condensation in cell physiology and disease. *Science* **357**, eaaf4382 (2017).
44. Zhou, R., Han, B., Xia, C. & Zhuang, X. Membrane-associated periodic skeleton is a signaling platform for RTK transactivation in neurons. *Science* **365**, 929–934 (2019).
45. Poliakov, A., Cotrina, M. L., Pasini, A. & Wilkinson, D. G. Regulation of EphB2 activation and cell repulsion by feedback control of the MAPK pathway. *J. Cell Biol.* **183**, 933–947 (2008).
46. Leonard, T. A., Loose, M. & Martens, S. The membrane surface as a platform that organizes cellular and biochemical processes. *Dev. Cell* **58**, 1315–1332 (2023).
47. Spencer, D. M., Wandless, T. J., Schreiber, S. L. & Crabtree, G. R. Controlling signal transduction with synthetic ligands. *Science* **262**, 1019–1024 (1993).
48. Groves, J. T. & Kuriyan, J. Molecular mechanisms in signal transduction at the membrane. *Nat. Struct. Mol. Biol.* **17**, 659–665 (2010).
49. Ghisleni, A. *et al.* Complementary mesoscale dynamics of spectrin and acto-myosin shape membrane territories during mechanoresponse. *Nat. Commun.* **11**, 5108 (2020).
50. Han, B., Zhou, R., Xia, C. & Zhuang, X. Structural organization of the actin-spectrin–based membrane skeleton in dendrites and soma of neurons. *Proc. Natl. Acad. Sci.* **114**, E6678–E6685 (2017).
51. Pan, L., Yan, R., Li, W. & Xu, K. Super-Resolution Microscopy Reveals the Native Ultrastructure of the Erythrocyte Cytoskeleton. *Cell Rep.* **22**, 1151–1158 (2018).
52. Ghisleni, A. *et al.* Complementary mesoscale dynamics of spectrin and acto-myosin shape membrane territories during mechanoresponse. *Nat. Commun.* **11**, 5108 (2020).
53. Ghisleni, A. *et al.* Mechanically induced topological transition of spectrin regulates its distribution in the mammalian cell cortex. *Nat. Commun.* **15**, 5711 (2024).
54. Belshaw, P. J., Ho, S. N., Crabtree, G. R. & Schreiber, S. L. Controlling protein association and subcellular localization with a synthetic ligand that induces heterodimerization of proteins. *Proc. Natl. Acad. Sci.* **93**, 4604–4607 (1996).
55. Putyrski, M. & Schultz, C. Protein translocation as a tool: The current rapamycin story. *FEBS Lett.* **586**, 2097–2105 (2012).
56. Taslimi, A. *et al.* An optimized optogenetic clustering tool for probing protein interaction and function. *Nat. Commun.* **5**, 4925 (2014).
57. Li, P. *et al.* Phase transitions in the assembly of multivalent signalling proteins. *Nature* **483**, 336–340 (2012).
58. Zhang, K., Zemke, N. R., Armand, E. J. & Ren, B. A fast, scalable and versatile tool for analysis of single-cell omics data. *Nat. Methods* **21**, 217–227 (2024).
59. Smith, M. P. *et al.* Reciprocal priming between receptor tyrosine kinases at recycling endosomes orchestrates cellular signalling outputs. *EMBO J.* **40**, e107182 (2021).

60. Snead, W. T. & Gladfelter, A. S. The Control Centers of Biomolecular Phase Separation: How Membrane Surfaces, PTMs, and Active Processes Regulate Condensation. *Mol. Cell* **76**, 295–305 (2019).

Supporting Information

A chemically inducible multimerization system for tunable and background-free RTK activation

Yuanmin Zheng[†1,2], Jinyu Fei[†1], Abhirup Chakrabarti[3], Ruobo Zhou[*1,2,3,4]

Affiliations: [1] Department of Chemistry, The Pennsylvania State University, University Park, PA 16802, USA

[2]Department of Biomedical Engineering, The Pennsylvania State University, University Park, PA 16802, USA

[3]Department of Biochemistry and Molecular Biology, The Pennsylvania State University, University Park, PA 16802, USA

[4]The Huck Institutes of Life Sciences, The Pennsylvania State University, University Park, PA 16802, USA

* To whom correspondence may be addressed. Email: ruobo.zhou@psu.edu

Experimental Procedures

Molecular cloning and plasmid construction

All plasmids and DNA fragments used in this study were obtained from Addgene or synthesized by commercial providers. Constructs were assembled using Gibson assembly (New England Biolabs, E5510S) according to the manufacturer's instructions.

The coding sequence for human FGFR1 was obtained from Addgene plasmid #116740. CRY2PHR (CRY2) and its oligomerization-prone mutant CRY2olig were derived from Addgene plasmid #106169. The Optodroplet system was constructed using Addgene plasmid #111507 as a backbone, in which the original FusionRed fluorophore was replaced with EGFP via PCR amplification and Gibson assembly. Cytoplasmic FGFR1 was fused at its C-terminus to CRY2, CRY2olig, or Optodroplet to generate the FGFR1–CRY2, FGFR1–CRY2olig, and FGFR1–Optodroplet constructs, respectively.

For the rapamycin-inducible clustering system, coding sequences for FKBP and FRB were obtained from Addgene plasmid #40896. The HOTag3 and HOTag6 multimerization domains were sourced from Addgene plasmids #106924 (FKBP–EGFP–HOTag3) and #106919 (FRB–EGFP–HOTag6), respectively. EGFP was replaced with mScarlet in both constructs by Gibson assembly to yield FKBP–mScarlet–HOTag3 and FRB–mScarlet–HOTag6. Additional variants incorporating alternative domain arrangements and linker lengths were assembled to generate constructs (Pairs 1 through 10) for systematic evaluation of FGFR1 clustering efficiency.

Cell culture and transfection

Human bone osteosarcoma epithelial cells (U2OS; ATCC HTB-96) were cultured in Dulbecco's Modified Eagle Medium (DMEM; Corning, 10-013-CV) supplemented with 10% (v/v) fetal bovine serum (FBS; Gibco, A52567-01) and 1% (v/v) penicillin–streptomycin (Gibco, 10378-016). Cells were maintained at 37 °C in a humidified incubator with 5% CO_2. For passaging, cultures were dissociated using 0.25% Trypsin–EDTA (Corning, 25-053-CI). For imaging experiments, cells were seeded onto 18-mm round glass coverslips (Electron Microscopy Sciences, 72222-01) placed in 12-well tissue culture plates.

Plasmid transfection was performed using TransIT®-LT1 reagent (Mirus Bio, MIR2300) according to the manufacturer's protocol. At 60–80% confluency, cells were transfected with 1.0 µg of plasmid DNA diluted in 100 µL of Opti-MEM (Gibco, 31985-070), followed by addition of 3 µL of TransIT-LT1 reagent. The mixture was incubated at room temperature for

15 min to allow complex formation, then added dropwise to the culture medium. After 6 h, the medium was replaced with fresh DMEM supplemented with 10% FBS to promote recovery and transgene expression. Cells were either imaged live or fixed for downstream analysis 24–48 h post-transfection, depending on the experimental protocol.

Blue light stimulation assay (Optogenetics)

For optogenetic clustering assays, U2OS cells expressing CRY2-based constructs were stimulated using a custom-built blue light system, as previously reported[1]. The setup consisted of a standard blue LED light source (465 nm) powered by a DC power supply. LED brightness was controlled to the desired level. Cells were stimulated with continuous blue light exposure for defined durations ranging from 30 seconds to 5 minutes, depending on the experimental conditions. To prevent unintended activation, samples were protected from ambient blue light prior to stimulation.

Live-cell imaging during stimulation was performed using Gibco™ Live Cell Imaging Solution (Thermo Fisher, A14291DJ), and cells were maintained at 37 °C throughout the assay. For fixed-cell experiments, light stimulation was followed by immediate fixation with 4% (w/v) paraformaldehyde (PFA) containing 4% (w/v) sucrose in phosphate-buffered saline (PBS) prior to immunostaining.

Rapamycin inducing assay

For fixed-cell assays, rapamycin (Millipore Sigma, Cat. No. 553210) was reconstituted in DMSO to a stock concentration of 100 mM, aliquoted, and stored at –20 °C. Before fixation, cells were treated with 500 nM rapamycin diluted in DMEM (with 10% FBS, 1% penicillin–streptomycin) and incubated at 37 °C for 30 minutes. Following stimulation, cells were immediately washed with PBS and fixed using 4% paraformaldehyde containing 4% sucrose in PBS for downstream immunostaining procedures.

For live-cell imaging assays, the 100 mM rapamycin stock was diluted to a final working concentration of 500 nM in Gibco™ Live Cell Imaging Solution (Thermo Fisher Scientific, Cat. No. A14291DJ). U2OS cells were pre-equilibrated by rinsing with pre-warmed imaging solution and incubating at 37 °C for at least 15 minutes prior to stimulation. Rapamycin was then added directly to the imaging chamber during acquisition, and time-lapse confocal imaging was performed over a 10–30 minute window post-treatment to monitor clustering dynamics.

Cell fixation and immunostaining for fluorescence imaging

U2OS cells grown on glass coverslips were fixed with 4% (w/v) PFA containing 4% (w/v) sucrose in PBS for 20 minutes at room temperature. After fixation, cells were rinsed three times with PBS and permeabilized with 0.2% (v/v) Triton X-100 in PBS for 10 minutes. Cells were then blocked with 3% (w/v) bovine serum albumin (BSA) in PBS for 1 hour at RT. Primary antibodies were diluted in blocking buffer and incubated with samples overnight at 4°C. The following day, cells were washed with PBS three times and incubated with fluorophore-conjugated secondary antibodies in blocking buffer for 1 hour at RT. After final washes in PBS, coverslips were mounted for imaging.

For immunostaining of phosphorylated ERK (p-ERK), U2OS cells were fixed at designated time points following light or rapamycin stimulation. Cells were first treated with 4% (w/v) PFA containing 4% (w/v) sucrose in PBS for 20 minutes at RT, followed by ice-cold methanol incubation at −20°C for 10 minutes. Samples were subsequently permeabilized with 0.2% Triton X-100 in PBS for 10 minutes and then subjected to blocking and antibody staining as described above.

For super-resolution imaging of βII-spectrin structures by STORM, U2OS cells were seeded on high-precision coverslips and fixed with 4% PFA and 4% sucrose in PBS, followed by the same immunostaining protocol as above. Antibody labeling was performed with fluorophores compatible with single-molecule localization microscopy. Imaging was conducted in dedicated STORM imaging buffer immediately following labeling.

The following primary antibodies were used in this study: mouse anti-βII spectrin antibody 1:200 dilution for immunofluorescence (Santa Cruz Biotechnology, sc-136074 or sc-515592); rabbit anti-phospho-ERK1/2 (Thr202/Tyr204) antibody 1:300 dilution for immunofluorescence (Cell Signaling Technology, 4370S). The following secondary antibodies were used in this study: Alexa Fluor-647-conjugated donkey anti-mouse IgG antibody 1:800 for IF (Jackson ImmunoResearch, 715-605-151); Alexa Fluor-647-conjugated donkey anti-rabbit IgG antibody 1:800 for IF (Jackson ImmunoResearch, 711-605-152).

Confocal imaging

Confocal imaging was performed on a custom microscope built on an Olympus IX-83 inverted body, equipped with a CrestOptics X-Light V3 spinning disk confocal unit. A 60× (NA 1.42) UPlanXApo or 100× (NA 1.40) UPlanSApo oil immersion objective (Olympus) was used in combination with an ORCA-Fusion BT digital CMOS camera (Hamamatsu, C15440-20UP).

Illumination was provided by a LDI-NIR-7 Laser Diode Illuminator (89 North), enabling sequential excitation of fluorophores including AF488 (or EGFP), mScarlet, and AF647.

3D-STORM imaging

Single-color three-dimensional stochastic optical reconstruction microscopy (3D-STORM) was performed using a custom-built setup based on a Nikon Eclipse-Ti2 inverted microscope, equipped with a 100× oil-immersion objective (NA 1.45, Plan Apo, Olympus) and an electron-multiplying CCD camera (Andor iXon Life 897). A 642-nm laser (MPB Communications Inc., 2RU-VFL-P-2000-642-B1R; 2000 mW) and 405-nm (Coherent, OBIS 405 nm LX, 1265577; 140 mW) was introduced through the rear port of the microscope and directed toward the edge of the objective to achieve near-total internal reflection (TIR) illumination, enabling selective excitation of fluorophores within a few microns of the coverslip surface.

For STORM imaging, Alexa Fluor 647 (AF647) was used as the reporter fluorophore. A cylindrical lens was inserted into the detection path to introduce point spread function ellipticity, allowing axial (z-axis) localization of single molecules based on the shape of their emission profile[2].

Cells were imaged in a standard oxygen-scavenging STORM imaging buffer composed of 100 mM Tris-HCl (pH 7.5), 100 mM cysteamine (Sigma-Aldrich), 5% (w/v) glucose, 0.8 mg/mL glucose oxidase (Sigma-Aldrich), and 40 μg/mL catalase (Sigma-Aldrich). AF647 molecules were continuously excited with the 642-nm laser (~2 kW/cm²), switching them into a non-fluorescent dark state. A low-intensity 405-nm laser was used for controlled reactivation to maintain a sparse population of active fluorophores suitable for single-molecule localization.

A typical 3D STORM image was reconstructed from ~30,000 frames acquired at 110 Hz. Image reconstruction and molecule localization were performed using previously established algorithms[2], rendering each localization as a 2D Gaussian peak centered at the estimated molecular position. Final images were visualized using custom MATLAB or ImageJ-based scripts.

Data quantification and analysis

All subsequent data quantification and analyses were performed using custom MATLAB scripts. To quantify the intensity of p-ERK and spectrin in transfected (EGFP-positive) cells, we first generated binary cell masks from the EGFP channel. The EGFP signal was smoothed using a Gaussian filter ($\sigma = 2$), followed by adaptive thresholding to generate binary masks. Hole filling was applied on a per-connected-component basis to ensure enclosed cellular regions were

captured. The resulting masks were further refined by removing small objects (<5000 pixels) and morphological closing. Individual cells were labeled, and corresponding p-ERK and spectrin images were loaded from the same field of view. For each labeled EGFP-positive cell, the mean and standard deviation (SD) of pixel fluorescence intensities were calculated within the segmented cell mask in each respective channel. The coefficient of variation (CV) was then computed as the ratio of SD to the mean fluorescence intensity, providing a measure of signal heterogeneity. In parallel, EGFP puncta were detected using a top-hat filter (disk size = 10 pixels) followed by a 99th percentile threshold and size filtering to exclude small artifacts (<3 pixels). Puncta counts, mean and SD values, and CVs for p-ERK and spectrin intensities in each cell were compiled and exported into Excel for downstream analysis.

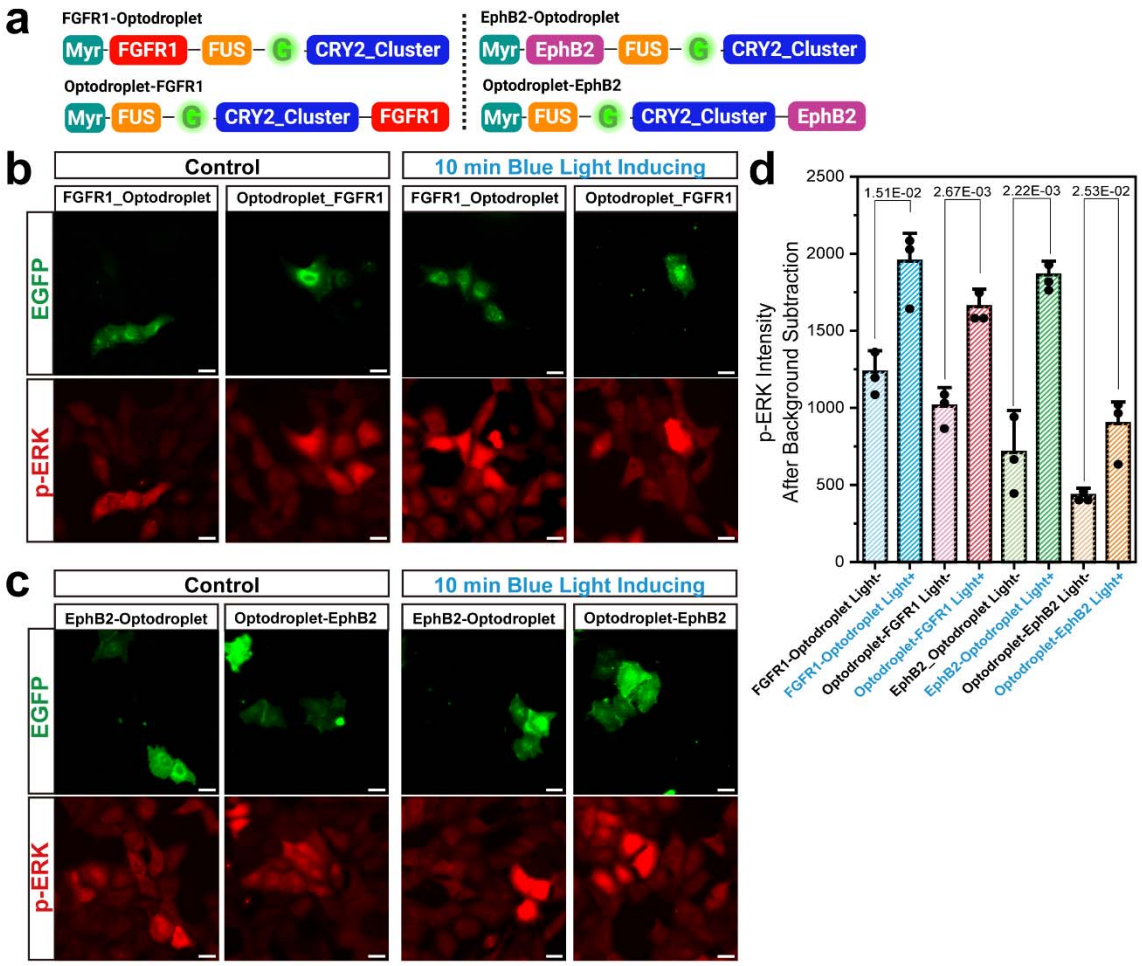

Fig. S1 Leaky ERK activation is independent of the optoDroplet module's N- or C-terminal position on RTK

a, Schematic diagrams of FGFR1 and EphB2 constructs with the optoDroplet module attached at the N- or C-terminus of RTK. **b and c,** Representative confocal immunofluorescence images of U2OS cells expressing FGFR1/EphB2-Optodroplet and Optodroplet-FGFR1/EphB2 constructs. All constructs were tagged with EGFP (green) and assessed for ERK pathway activation using immunostaining for p-ERK (red) under dark (control) and light-inducing conditions. Scale bars, 20 μm**. d,** Quantification of average total p-ERK fluorescence intensity in transfected cells under control and light-stimulating conditions. Fluorescence intensities were background-subtracted using signals from neighboring untransfected cells and presented as mean ± s.d. from n = 3 biological replicates. Individual data points represent averaged values from independent imaging fields.

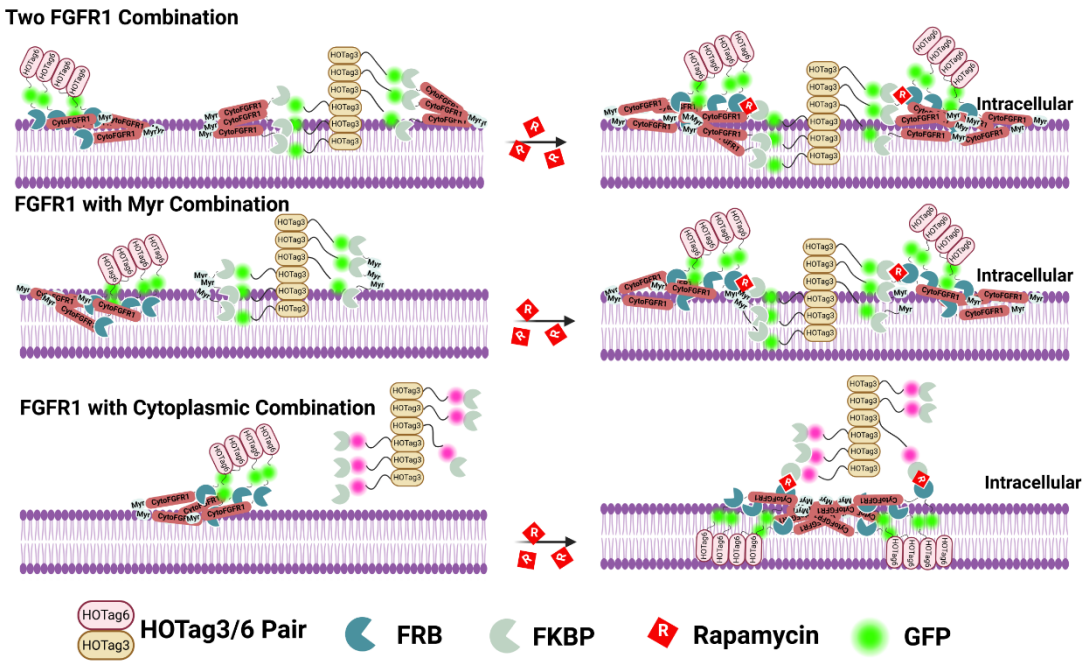

Fig. S2 Schematic diagrams of three chemical-inducible RTK activation strategies

Mechanistic illustrations of three classes of chemically inducible FGFR1 clustering designs. All systems utilize rapamycin-induced FKBP–FRB heterodimerization to drive higher-order multimerization coupled to HOTag3 and HOTag6 coiled-coil domains. **Top panel:** Membrane-tethered designs (Pairs 1–2), in which both FGFR1 fusion components are anchored to the plasma membrane and contain multimerization domains. These configurations promote strong receptor clustering but exhibit relatively high basal activity, potentially resulting from the high effective concentration of FGFR1 at the two-dimensional membrane. **Middle panel:** Asymmetric membrane–membrane designs (Pairs 3–6), in which one fusion construct lacks the FGFR1 kinase domain but remains membrane-anchored. These constructs reduce basal clustering but show weak ERK activation upon stimulation, potentially due to constrained clustering geometry preventing the higher-order FGFR1 multimerization. **Bottom panel:** Asymmetric membrane–cytosolic designs (Pairs 7–10), where FGFR1 fusion constructs are membrane-localized while interacting partners reside in the cytosol. Rapamycin induces interfacial assembly at the membrane, enabling tunable clustering with minimal background activity. Optimal signaling output is achieved with balanced multimerization strength and spatial separation. Created in BioRender. Zheng, Y. (2025) https://BioRender.com/5i7pvbv

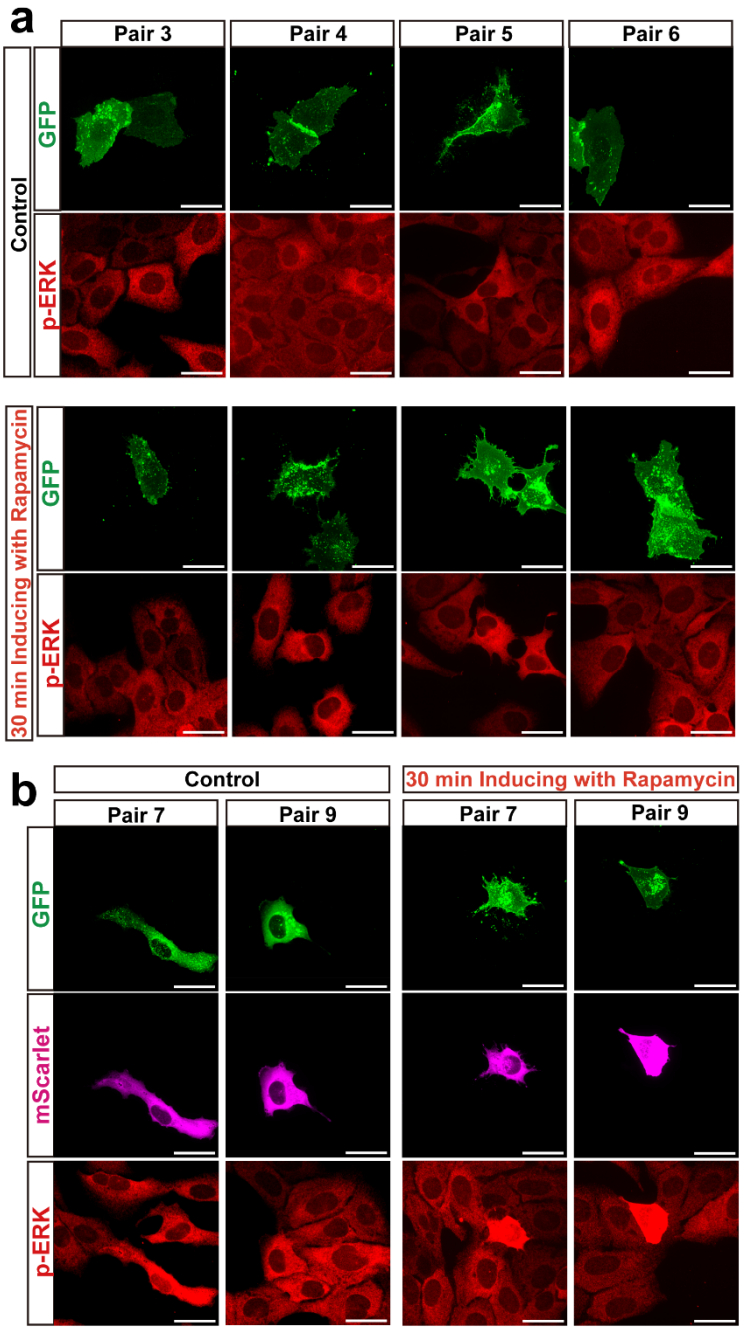

Fig. S3 ERK activation of additional rapamycin-inducible designs

U2OS cells were transfected with the indicated FGFR1 constructs from screening Pairs 3-6, 7 and 9, and imaged under basal conditions or following 30-minute stimulation with 500 nM rapamycin. Each construct was tagged with EGFP (green) to visualize expression and clustering behavior. ERK activation was assessed via immunostaining for p-ERK (red). Cells expressing Pair 7 and Pair 9 also included mScarlet-tagged components (magenta) to distinguish membrane-localized and cytosolic modules. Constructs showed variable levels of basal ERK signal and

inducible ERK activation depending on clustering configuration and multimerization strength. Scale bars, 10 μm.

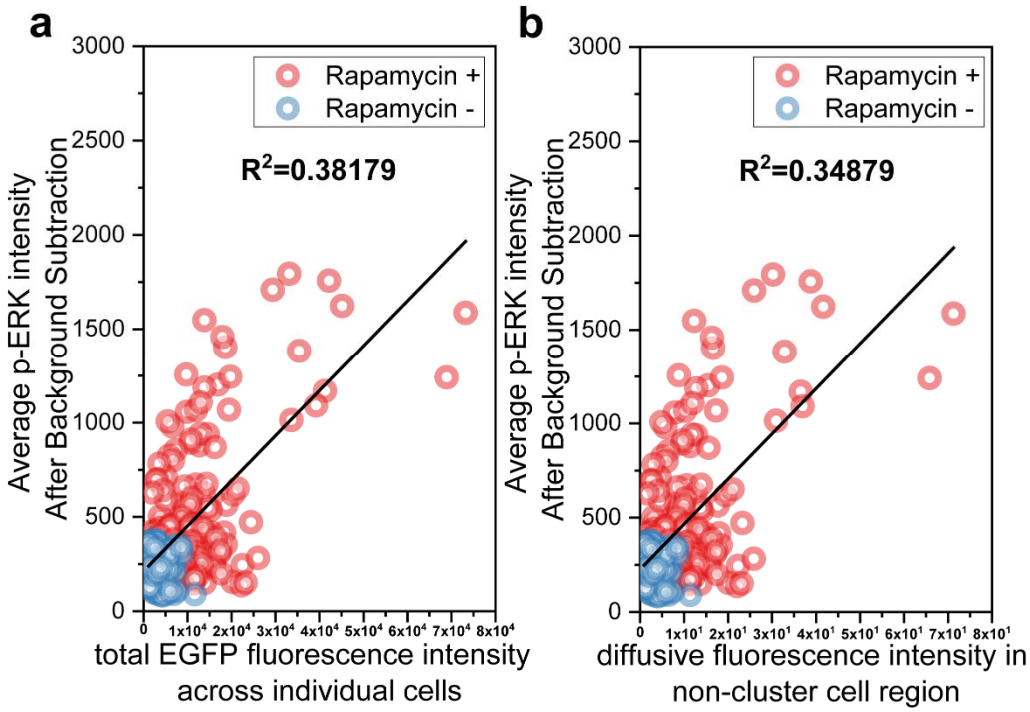

Fig. S4 Single-cell correlation of FGFR1 measures with p-ERK

a. Correlation between total EGFP fluorescence intensity (i.e., the total FGFR1 amount in each cell) and total p-ERK fluorescence intensity across individual cells. **b.** Correlation between the diffusive fluorescence intensity in non-cluster cell region (i.e., the FGFR1 amount outside FGFR1 clusters the in each cell) and total p-ERK fluorescence intensity across individual cells. Linear regression analysis shows these correlations are markedly lower than the correlation between FGFR1 amount within FGFR1 clusters and total p-ERK fluorescence intensity across individual cells, indicating that p-ERK activation is primarily driven by FGFR1 clusters rather than by diffusive, unclustered FGFR1.

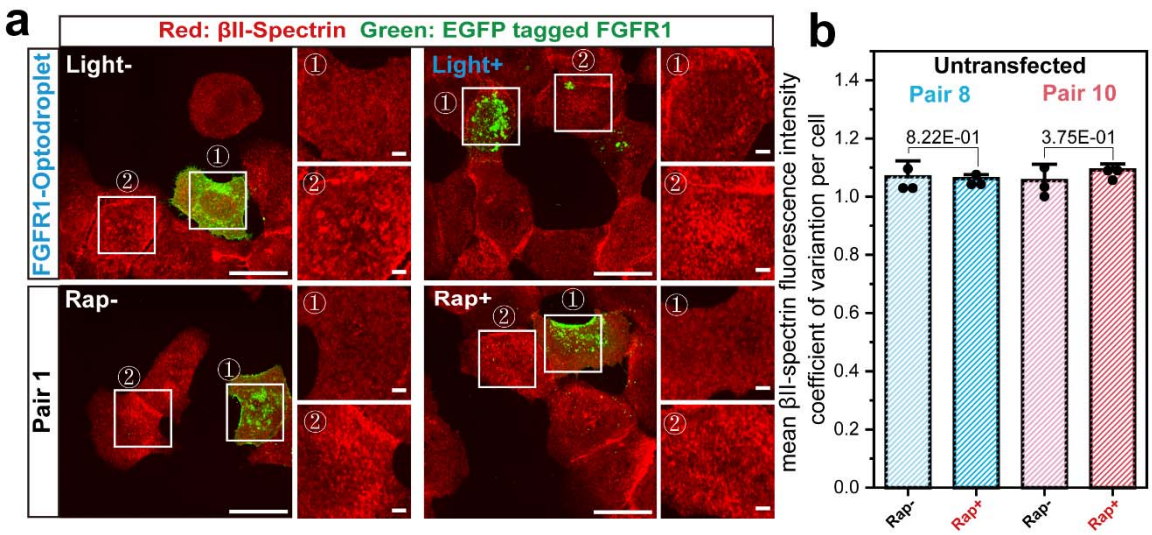

Fig. S5 Spectrin degradation in cells expressing optogenetic and chemically inducible FGFR1 constructs with considerable basal ERK activation.

a. Representative immunofluorescence images of U2OS cells expressing either FGFR1-Optodroplet (top row) or rapamycin-inducible FGFR1 Pair 1 (bottom row), shown under control and stimulated conditions. Cells were stained for endogenous βII-spectrin (red) to assess cytoskeletal integrity. White boxed regions highlight transfected ① and adjacent untransfected ② cells from the same field of view. Optogenetic constructs were stimulated with blue light for 10 minutes, and rapamycin-treated cells were incubated with 500 nM rapamycin for 30 minutes prior to fixation. In both groups, spectrin signal was substantially reduced in transfected cells following activation, whereas neighboring untransfected cells retained intact spectrin architecture. Scale bars, 10 μm (Original view), 2 μm (Cropped view). **b.** mean coefficient of variation (CV) of βII-spectrin fluorescence intensity for untransfected cells, used as a proxy for spatial heterogeneity and cytoskeletal patterning. Cells with intact spectrin networks exhibit high CVs due to alternating bright/dark regions, and spectrin-disrupted cells show reduced CV. Values are mean ± s.d. from three biological replicates. p-values are calculated using a two-sided unpaired Student's T-test.

References

1. Krishnamurthy, V. V. *et al.* Light-mediated Reversible Modulation of the Mitogen-activated Protein Kinase Pathway during Cell Differentiation and Xenopus Embryonic Development. *J. Vis. Exp. JoVE* 55823 (2017) doi:10.3791/55823.
2. Huang, B., Wang, W., Bates, M. & Zhuang, X. Three-Dimensional Super-Resolution Imaging by Stochastic Optical Reconstruction Microscopy. *Science* **319**, 810–813 (2008).